

# Visualization and Performance Metric in Many-Objective Optimization

Zhenan He and Gary G. Yen, *Fellow, IEEE*

**Abstract**—Visualization of population in a high-dimensional objective space throughout the evolution process presents an attractive feature that could be well exploited in designing many-objective evolutionary algorithms (MaOEAs). In this paper, a new visualization method is proposed. It maps individuals from a high-dimensional objective space into a 2-D polar coordinate plot while preserving Pareto dominance relationship, retaining shape and location of the Pareto front, and maintaining distribution of individuals. From it, a decision-maker can observe the evolution process, estimate location, range, and distribution of Pareto front, assess quality of the approximated front and tradeoff between objectives, and easily select preferred solutions. Furthermore, its applications can be scalable to any dimensions, handle a large number of individuals on front, and simultaneously visualize multiple fronts for comparison. Based on this visualization tool, a performance metric, named polar-metric, is designed. The convergence of the approximate front is measured by radial values of all population members on that front. Meanwhile, the diversity performance is mainly determined by niche count of each subregion in a high-dimensional objective space. Experimental results show that it can provide a comprehensive and reliable comparison among MaOEAs.

**Index Terms**—Many-objective evolutionary algorithm (MaOEA), many-objective optimization problem (MaOP), mapping, performance metric, visualization.

## I. INTRODUCTION

**M**ANY real-world multiobjective optimization problems (MOPs) involve more than three conflicting objectives, which are commonly referred to as many-objective optimization problems (MaOPs). Visualization of population in a high-dimensional objective space throughout the evolution process presents an opportunity that could be well exploited in designing many-objective evolutionary algorithms (MaOEAs). High-quality visualization tools can provide accurate shape, location, and range of the approximate Pareto front, reflect tradeoffs between objectives, observe the evolution process, assess the quality of the approximated front, and help decision-makers select their preferred solutions [1]. In low-dimensional spaces with two or three objectives, scatter plot shows the location, distribution, and shape of the obtained approximate front,

where each axis directly represents one objective. From scatter plot, a decision-maker can easily make choices and select preferred solutions if so desired. However, due to the curse of dimensionality, it is no longer an option in high-dimensional objective spaces.

Naturally, we thought about developing strategies to reduce the number of objectives while preserving as much information of all objectives as possible. If the number of objectives is reduced to be two or three, then we can easily visualize the approximate Pareto front by a scatter plot. For instance, Brockhoff and Zitzler [2] first identified conflict and nonconflict relationships between each pair of objectives and then combine nonconflicting objectives into one objective. Saxena *et al.* [3] presented a principal component analysis and maximum variance unfolding based framework for linear and nonlinear objective reduction algorithms, respectively. Lygoe *et al.* [4] exploited local harmony between objectives to reduce dimensionality by clustering the Pareto-optimal front and apply a rule-based principal component analysis including preference articulation for potential objective reduction. However, there are many problems whose objectives cannot be further reduced. Moreover, in some problems, eliminating a very small number of objectives does not help for visualization.

In this paper, there are many visualization approaches designed for viewing high-dimensional data. The first type of methods, including various forms of parallel coordinates [5] and heatmaps [6], represents each high-dimensional solution on a parallel coordinate system. For an  $M$ -dimensional objective space, the whole parallel coordinate system contains  $M$  parallel axes, each of which corresponds to one objective. This method can only retain the original objective values of solutions. In order to provide information about the trade-off relationships between objectives for a decision-maker, it requires the objectives of interest to be positioned adjacent to each other. However, the number of comparisons among different adjacent objectives would grow exponentially with the number of objectives. In addition, it is not able to show the contour information of a given approximate Pareto front [1]. The second type of methods, including Buddle chart [7], radial coordinate visualization (RadViz) [8], self-organizing maps (SOMs) [9], Sammon mapping [10], and neuroscale [11], constructs the mapping from a high-dimensional objective space into a 2-D space while preserving local distances between each pair of solutions in a high-dimensional space. From the 2-D space, decision-makers can easily determine their preferred solutions. However, these

Manuscript received October 15, 2014; revised March 24, 2015 and June 17, 2015; accepted August 20, 2015. Date of publication August 24, 2015; date of current version May 26, 2016.

The authors are with the School of Electrical and Computer Engineering, Oklahoma State University, Stillwater, OK 74075 USA (e-mail: zhenan@okstate.edu; gyyen@okstate.edu).

Color versions of one or more of the figures in this paper are available online at <http://ieeexplore.ieee.org>.

Digital Object Identifier 10.1109/TEVC.2015.2472283

mapping approaches often inadvertently lose some critical information in the mapped 2-D space. Furthermore, in the mapped 2-D space, it is still not intuitive to discover the shape of the approximate front and tradeoffs between objectives. Based on the above discussions, it remains difficult to visualize Pareto front approximations using present technologies. An effective visualization method is needed to provide accurate and comprehensive information for the approximate Pareto front in high-dimensional objective spaces.

On the other hand, there is no performance metric specifically designed for comparison of MaOEA in high-dimensional MaOPs. In this paper, there are many effective performance metrics used to compare multiobjective evolutionary algorithms (MOEAs) in low-dimensional MOPs. Most of these metrics are originally designed for low-dimensional problems. Even so, Okabe *et al.* [12] have showed that many metrics may fail to truly reflect the quality of solution sets and some metrics work only for bi-objective optimization problems. When comes to high-dimensional objective spaces, these metrics cannot perform faithfully as in the low-dimensional spaces. In [13], we have applied an ensemble method for comparison of MaOEAs as any performance metric alone cannot quantify the performance of an MaOEA comprehensively. Although this ensemble method has shown its powerful ability in providing a comprehensive measure, it still uses multiple metrics mainly designed for low-dimensional MOPs. Therefore, in high-dimensional objective space, performance metric ensemble based on existing performance metrics cannot provide convincing comparison results. There still needs a comprehensive study to reveal the strengths and weaknesses of the underlying MaOEAs.

In this paper, a new visualization method for high-dimensional objective spaces is designed. It maps individuals from a high-dimensional space into a 2-D polar coordinate system with pole (0, 0), where each individual is assigned a radial coordinate value and an angular coordinate value. Radial coordinate reflects convergence performance of each individual and it is determined by the original objective value of each individual and the shape of the approximate front in a high-dimensional space. The smaller the radial coordinate value, the closer the distance is to the true Pareto front. On the other hand, angular coordinate reveals distribution of individuals on the approximate front. It also shows crowdedness in each subregion of a high-dimensional space. The more number of different angular coordinate values among all individuals, the better distribution and spread of the approximate front is.

This method retains Pareto dominance relationship between individuals on the approximate Pareto front, preserves shape and location of Pareto front, and maintains distribution of solutions. From it, decision-makers can observe the evolution process, estimate location, range, and distribution of Pareto front, assess the quality of the approximate front and tradeoff between objectives, and easily select their preferred solutions. This design can be scalable to any dimensions, handle a large number of individuals on the approximate front, and simultaneously visualize multiple fronts for the purpose of visual comparison. Moreover, the resulted visualization plot is insensitive to the addition or removal of an individual.

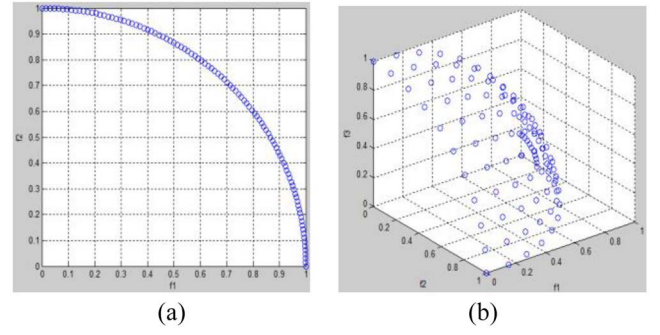


Fig. 1. Scatter plot in (a) 2-D and (b) 3-D spaces.

Based on this proposed visualization approach, a performance metric called polar-metric ( $p$ -metric) is designed to quantify the performance of MaOEAs. The convergence of the approximate front is measured by radial values of all population members on that front, which are the result of a scalarization function. Meanwhile, the diversity performance of the approximate front is mainly determined by niche count of each subregion in a high-dimensional space. Experiment results show that  $p$ -metric with robust characteristic makes comparative results a quality indicator of the evaluated MaOEAs.

The remaining sections complete the presentation of this paper. Section II outlines selected literature for both existing visualization approaches and performance metrics. Section III elaborates on the proposed visualization method in detail and the design of new performance metric,  $p$ -metric, based on the visualization approach proposed. Section IV details the experimental setting and findings for selected scalable benchmark problems. Finally, the conclusion is drawn in Section V along with pertinent observations. Without loss of generality, in the remaining paper, we only consider the minimization problems.

## II. LITERATURE SURVEY

In this section, we summarize both popular visualization approaches available for MaOPs and performance metrics designed specifically for evaluation of MaOEAs.

### A. Popular Visualization Approaches for MaOPs

In a low-dimensional space with two or three objectives, a scatter plot shows the location, distribution, and shape of the approximated front, where each axis directly represents one objective. From a scatter plot, a decision-maker easily makes choices and picks up preferred solutions. However, it cannot be extended to high-dimensional objective spaces with more than 3-D. As an extension of scatter plot, Buddle chart [7] uses size and color to represent the fourth and fifth dimensions, respectively, so that the number of visualization dimensions is limited to five. Fig. 1 shows examples of scatter plot in 2-D and 3-D objective spaces, respectively.

In this paper, there are two types of visualization methods designed for visualizing high-dimensional data. The first type of methods, including parallel coordinates [5] and

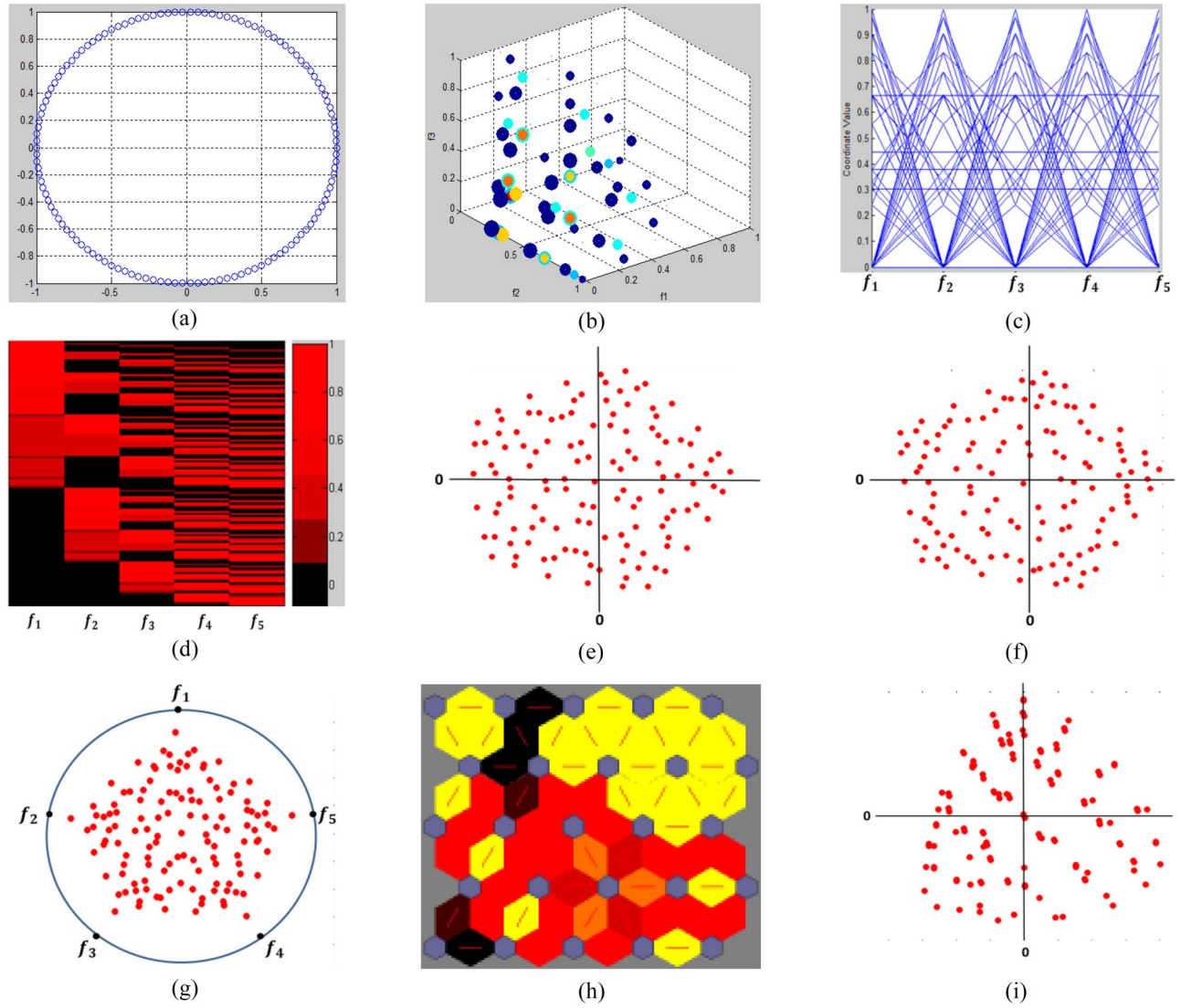


Fig. 2. Visualization of the true Pareto front of 5-D DTLZ2 using different visualization methods. (a) Our proposed method. (b) Buddle chart. (c) Parallel coordinates. (d) Heatmap. (e) Sammon mapping. (f) Neuroscale. (g) RadViz. (h) SOM. (i) Isomap.

heatmaps [6], represents each high-dimensional solution on a parallel coordinate system. The second type of methods, including RadViz [8], SOM [9], Sammon mapping [10], and neuroscale [11], constructs the mapping from a high-dimensional objective space into a 2-D space while preserving local distances and Pareto dominance relationship between each pair of individuals in a high-dimensional space. Fig. 2 shows visualization of the true Pareto front (with the population size 126) of 5-D DTLZ2 using all these existing visualization methods and our proposed method (to be discussed in Section III).

1) *Visualization Based on Parallel Coordinate System*: For an  $M$ -dimensional objective space, the respective parallel coordinate system would contain  $M$  parallel axes, each of which represents one objective. This method can directly show the original objective values of solutions, does not require sophisticated mappings of vector, and can be easily scaled into higher dimensions. In the objective space, if objectives of interest are positioned adjacent to each other, this method can also provide information about the tradeoff relationships between objectives

and contour information of the approximate Pareto front for decision-maker.

a) *Parallel coordinates* [5]: Each  $M$ -dimensional vector is represented by a polyline with vertices on the parallel axes, where each axis represents one objective and the position of the vertex on each axis equals to the objective value in that dimension [1]. The most appreciable benefit of parallel coordinates is clearly representing dependences between objectives. However, each individual needs one polyline and there will be many polylines if the number of individuals is large. There exist creative ways to address the issue of over-crowded lines, such as [39].

b) *Heatmap* [6]: Similar to parallel coordinates, heatmap still uses parallel axes where each axis represents 1-D. However, in a heatmap, objective values are shown using color while they are represented by polyline in parallel coordinates. A heatmap cannot show tradeoffs between objectives, either. Meanwhile, the increasing number of solutions requires more and more colors to be used and it is not easy to visually distinguish among such a large number of colors.



2) *Visualization Based on Mapping*: This type of methods uses some more sophisticated mapping techniques to perform dimension reduction to the 2-D space. All mapping methods try to preserve Pareto dominance relationship among individuals in a high-dimensional space and retain local distances between each pair of them, where relative distances between the representations of individuals in the visualization space are required to be as close as possible to those in the original objective space [14]. They are also scalable to many dimensions. However, they are often computationally expensive and not robust as the mapping heavily depends on the values of the objective vectors in the approximate front. Meanwhile, all kinds of mapping methods cannot avoid losing some important information in a high-dimensional space. Furthermore, in the mapped 2-D space, it is still not easy to discover the shape of the approximate front and tradeoffs between objectives.

a) *Sammon mapping* [10] and *neuroscale* [11]: Both approaches minimize the stress function to preserve the local distances. In Sammon mapping, the minimization can be performed either by gradient descent, or by other iterative methods. It can also preserve the well distribution of solutions. Neuroscale retains distances using a radial basis function neural network to minimize the stress function.

b) *Radial coordinate visualization* [8]: The idea of RadViz is originated from physics. In RadViz, objectives represented as dimensional anchors are distributed evenly on the circumference of the unit circle. Each individual is held with springs attached to the anchors and the spring force is proportional to the value in the corresponding objective. The position of the individual is located on where the spring forces are in equilibrium. For example, solutions that are placed close to one anchor have a higher value in that objective than in any other objectives, while solutions with all equal values in all dimensions are placed exactly in the center of the circle. It is able to preserve well the distribution of vectors but it cannot distinguish the shape of the approximate Pareto fronts.

c) *Self-organizing map* [9]: The SOMs are one type of artificial neural networks providing a topology preserving mapping from  $M$ -dimension ( $M > 2$ ) to a lower dimension (usually 2-D). Nearby vectors in the input high-dimensional space are mapped to nearby units (neurons) in SOMs. The neuron can be hexagonal grid [15]. When trained, SOMs can be visualized using a unified distance matrix, where the distance between adjacent neurons is presented with different colorings. Light areas represent clusters of similar neurons and dark areas indicate cluster boundaries.

d) *Isomap* [16]: Isomap preserves the intrinsic geometry of solutions when mapping to 2-D space using multidimensional scaling [17], where each solution is linked only to its closest neighbors. The geodesic distance between both of them is calculated as the sum of Euclidean distances of the shortest path between them.

## B. Existing Performance Metrics for MaOEAs

Performance metrics can be broadly divided into five different categories according to the optimization goals [13].

The first category involves metrics assessing the number of Pareto optimal solutions in the set: ratio of nondominated individuals (RNI) [18] measures the proportion of the nondominated solutions found with respect to the population size; error ratio [19] checks the proportion of nontrue Pareto points in the approximate front over the population size; overall nondominated vector generation [19] simply counts the number of distinct nondominated individuals found; and the  $n$ -ary performance metric, pareto dominance indicator [20], measures the ratio of nondominated solutions contributed by a particular approximate front to the nondominated solutions provided collectively by all approximate fronts. Within the second category, metrics measuring the closeness of the solutions to the theoretical true Pareto front for a given benchmark function are given: generational distance (GD) [19] measures how far the evolved solution set is from the true Pareto front; a complementary metric of GD called inverted GD (IGD) [21] concerns how well is the Pareto-optimal front represented by the obtained solution set; and maximum pareto front error [19] focuses on the largest distance between the individual in the theoretical Pareto front and the points in the approximation front. In the third category, metrics are relating on distribution of the solutions: uniform distribution [18] quantifies the distribution of an approximate front under a predefined parameter; spacing [22] measures how evenly the evolved solutions distribute themselves; and the number of distinct choices [23] identifies solutions that are sufficiently distinct for a special parameter  $\mu$ . Fourth, metrics concerning spread of the solutions are included: maximum spread (MS) [24] measures how well the true Pareto front is covered by the approximation set. In the last category, metrics consider both closeness and diversity at the same time: hyperarea and ratio (or  $S$ -metric) [24], [25] calculate the volume covered by the approximate front with respect to a properly chosen reference point.

However, in high-dimensional objective spaces, these metrics cannot perform as well as in the low-dimensional spaces. For example, spacing is very effective to measure the distribution of the approximate front in low-dimensional MOPs by calculating the distance between each individual and its closest neighbor. However, in a high-dimensional space, it is difficult to identify this closest neighbor due to a large objective space requiring a heavier computation workload. The IGD which calculates the distance between each individual in the true Pareto front and its closest individual in the approximate front for a given MaOP also suffers this difficulty. Furthermore,  $S$ -metric can measure both convergence and diversity performances in low-dimensional spaces, but in high-dimensional MaOPs, the calculated volume cannot reflect the distribution of the approximate Pareto front very well. Moreover, it is fairly computational expensive for an MaOP. For MS metric, it may prefer the nonconverged approximate front than the converged but not well spread front in an MaOP. Finally, in a high-dimensional space, nearly all individuals are non-dominated with respect to each other [26]. As a result, the metric RNI cannot provide much useful evaluation result in MaOPs.

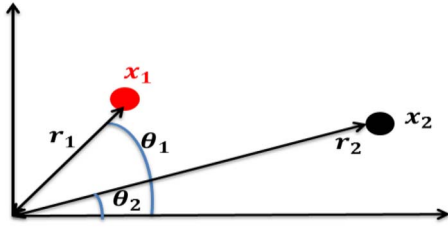


Fig. 3. 2-D polar coordinate system.

### III. PROPOSED METHOD

In this section, first a new visualization method for the approximate Pareto front in a high-dimensional space is proposed. Then, based on this visualization approach, a new performance metric, called  $p$ -metric, is developed specifically for evaluating MaOEAs in both convergence and diversity performances in a high-dimensional objective space.

#### A. Visualization Method

A new visualization method that preserves Pareto dominance relationship between individuals on the approximated Pareto front, retains shape and location of Pareto front, and maintains distribution of solutions is proposed herein. From it, decision-makers can monitor the evolution progress, estimate location, range, and distribution of approximate Pareto front, assess quality of the approximate front and tradeoff between objectives, and easily select their preferred solutions. This design can be scalable to any dimensions, handle a large number of individuals on the approximate front, and simultaneously visualize multiple fronts, if so desired, for visual comparison. Moreover, it is insensitive to the addition or removal of a vector.

By this design, individuals are mapped from a high-dimensional Cartesian space into a 2-D polar coordinate system with pole  $(0, 0)$ . Each individual is assigned a radial coordinate value and an angular coordinate value in this polar coordinate system. The radial coordinate of one individual reflects its convergence status and is determined by both its original objective values and the shape of the approximate front in a high-dimensional space. Angular coordinates of all individuals show distribution of individuals on the approximate front and the crowdedness in each subregion of a high-dimensional space. Fig. 3 shows an example of a 2-D polar coordinate system. For solution  $x_1$ , its radial coordinate value is  $r_1$  and angular coordinate value is  $\theta_1$ . For solution  $x_2$ , its radial coordinate value is  $r_2$  and angular coordinate value is  $\theta_2$ .

1) *Visualization Based on Mapping*: Fig. 4 shows the complete mapping process. First, the original high-dimensional objective space is equally divided into  $N$  subregions, each of which is represented by one direction vector so that all direction vectors are evenly distributed. Then, each direction vector is mapped as one 2-D vector called mapped direction vector in a 2-D polar coordinate system. In this 2-D space, each mapped direction vector is assigned an angular coordinate value  $\theta$ . Table I shows an example of the mapping process from a 3-D space to a 2-D space. Here, the original 3-D space

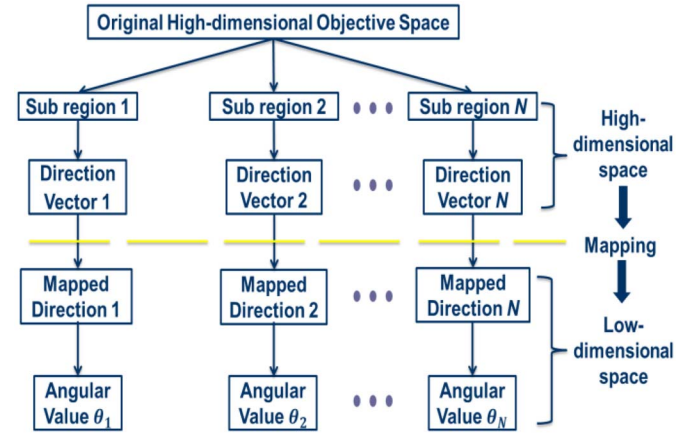


Fig. 4. Proposed mapping process.

TABLE I  
MAPPING FROM 3-D TO 2-D SPACES

Sub Region (3D)	Direction Vector (3D)			Mapped Direction (2D)	$\theta_i$ (2D)
1	0	0	1	$v_1$	$0^\circ$
2	0	0.25	0.75	$v_2$	$24^\circ$
3	0	0.5	0.5	$v_3$	$48^\circ$
4	0	0.75	0.25	$v_4$	$72^\circ$
5	0	1	0	$v_5$	$96^\circ$
6	0.25	0	0.75	$v_6$	$120^\circ$
7	0.25	0.25	0.5	$v_7$	$144^\circ$
8	0.25	0.5	0.25	$v_8$	$168^\circ$
9	0.25	0.75	0	$v_9$	$192^\circ$
10	0.5	0	0.5	$v_{10}$	$216^\circ$
11	0.5	0.25	0.25	$v_{11}$	$240^\circ$
12	0.5	0.5	0	$v_{12}$	$264^\circ$
13	0.75	0	0.25	$v_{13}$	$288^\circ$
14	0.75	0.25	0	$v_{14}$	$312^\circ$
15	1	0	0	$v_{15}$	$336^\circ$

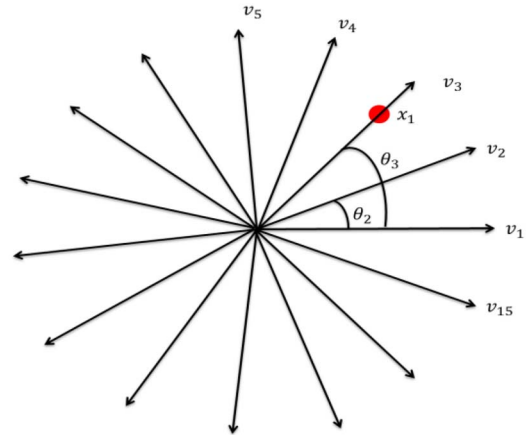


Fig. 5. Mapped 2-D space.

is evenly divided into 15 subregions. The mapped 2-D space is shown in Fig. 5, where each mapped direction ( $v_1, v_2, \dots$ , and  $v_{15}$ ) is assigned a fixed angular coordinate value ( $\theta_1, \theta_2, \dots$ , and  $\theta_{15}$ ), respectively. Meanwhile, each  $v_i, i = 1 : 15$  represents one subregion in the original high-dimensional space. For example, individual  $x_1$  on the subregion of high-dimensional

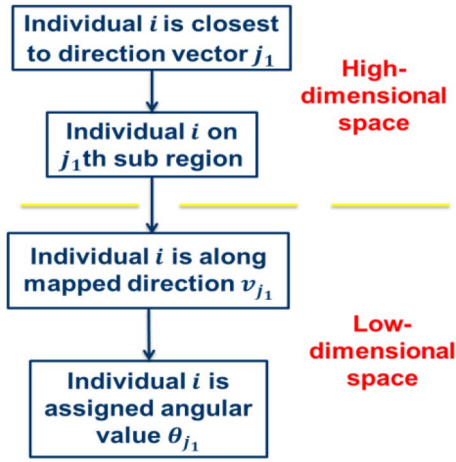


Fig. 6. Angular coordinate value assignment for each individual.

space corresponding to  $v_3$  is assigned the angular value  $\theta_3$  (i.e.,  $48^\circ$ ) in the mapped 2-D space.

Note that, on this 2-D polar coordinate system, the order of direction vectors is only determined by the order to generate them in the original high-dimensional space, where the generating process is shown in Table I. That is, even though two direction vectors are closest to each other in a 2-D polar coordinate system, they may not be closest to each other in the original high-dimensional space, e.g.,  $v_9$  and  $v_{10}$  in Fig. 5. On the other hand, the distribution performance of the whole approximate front can only be measured by checking the difference of crowdedness among direction vectors. If two solutions are mapped into different directions in a 2-D polar coordinate system, we cannot directly derive their relative distance by looking at the mapped 2-D space. For example, if a solution is located at the direction of  $v_9$  in the 2-D polar coordinate system, it only implies that this solution is located in the subregion specified by  $v_9$  and it cannot provide any information that the relative distance between this solution to another direction vectors  $v_{10}$  or  $v_{11}$  in the high-dimensional space. Furthermore, we do not consider about the distribution of solutions within each direction vector because solutions in the same direction vector are assigned the same angular value.

2) *Calculation of Angular Coordinate Value:* From the last section, a group of equally distributed direction vectors are predefined in a high-dimensional space, each of which specifies a unique subregion in a high-dimensional objective space. Then, each vector is mapped to the 2-D space and assigned a fixed angular coordinate value. For each individual in high-dimensional space, its angular coordinate value in the 2-D polar coordinate system is the same as the value of its closest direction vector in the original high-dimensional space. Fig. 6 shows the process of how to assign the angular coordinate value for each individual. If more solutions share the same angular coordinate, then they are crowded in one subregion. Thus, they have a poor diversity performance. Furthermore, if two solutions have very close radial and angular values, then they are very close to each other in the original high-dimensional space.

3) *Calculation of Radial Coordinate Value:* From the first two sections, we have known how to assign angular coordinate

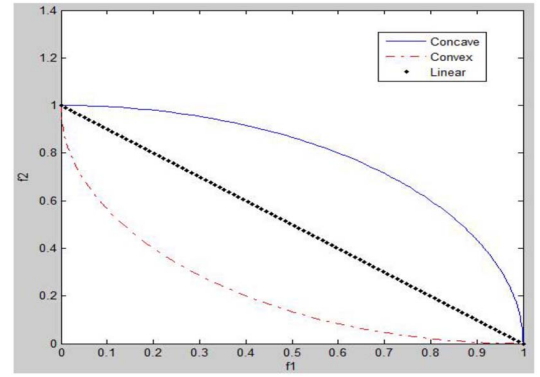


Fig. 7. Three basic geometric types of Pareto fronts.

value for each individual in the mapped 2-D space. In this part, we will assign radial coordinate value for each individual in the mapped 2-D space.

In this paper, there are three basic geometric shapes of Pareto fronts for an MaOP. They are concave, convex, and linear. From [26], a Pareto front is concave if and only if it is covered by its convex hull. On the other hand, a convex Pareto front implies that it covers its convex hull. Furthermore, a linear front neither covers its convex hull nor be covered by its convex hull. These three types of Pareto fronts in a two-objective problem are shown in Fig. 7.

Based on three basic shapes, a mixed front would contain multiple subparts with different types of geometries. For example, one mixed front can be a combination of convex and linear. On the other hand, a degenerated front is of lower dimension than objectives space where it is embedded [22] and a disconnected front means that the front is not continuous across the objective space. Here, similar to a mixed front, degenerated front and disconnected front can still be generated by the combination of three basic shapes. Therefore, we focus only on the mapping of these three fundamental types of fronts from a high-dimensional space to the mapped 2-D space.

In an  $M$ -dimensional optimization problem, when the Pareto front is concave, there is a constant  $r$  such that  $\sum_{m=1}^M (f_m(x))^2 = r^2$  for any solution  $x$  on the true Pareto front, where the objective value of  $x$  is presented as  $[f_1(x), f_2(x), \dots, f_M(x)]$ . When the Pareto front is convex, there is also a constant  $r$  such that  $\sum_{m=1}^M (r - f_m(x))^2 = r^2$  for any solution  $x$  on that true Pareto front. For the linear Pareto front, there exists a constant  $r$  such that  $\sum_{m=1}^M f_m(x) = r$  for any solution  $x$  on the true Pareto front. The constant  $r$  can be directly used to evaluate the convergence performance of each individual on different shape of fronts. For the minimization problem, the lower the value of  $r$ , the better the convergence performance is. Figs. 8–10 show different  $r$ 's under three different shapes of fronts within a two-objective space (the original space without mapping) for the purpose of visualization only. Under all geometric shapes, the Pareto front with radial coordinate value  $r_1$  has a better convergence performance than that of Pareto front with  $r_2$  because  $r_1$  is smaller than  $r_2$  in all three cases.

Furthermore, this mapping process provides a way to visualize the shape of the approximate front in a high-dimensional



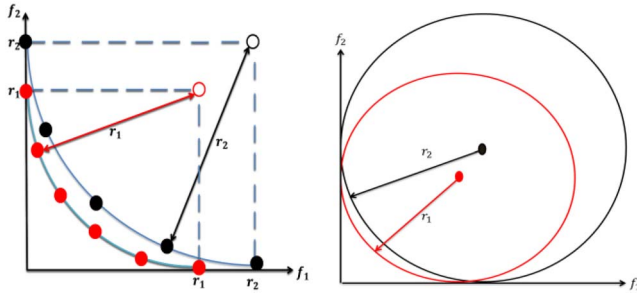


Fig. 8.  $r$  in convex front:  $\sum_{m=1}^M (r - f_m(x))^2 = r^2$ .

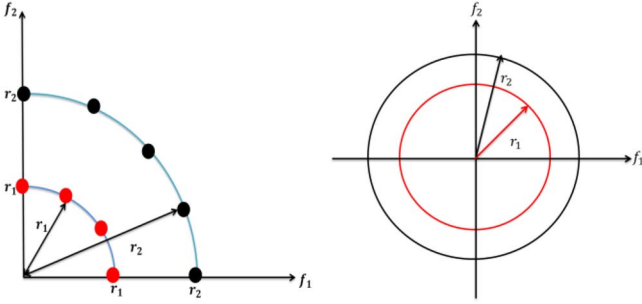


Fig. 9.  $r$  in concave front:  $\sum_{m=1}^M (f_m(x))^2 = r^2$ .

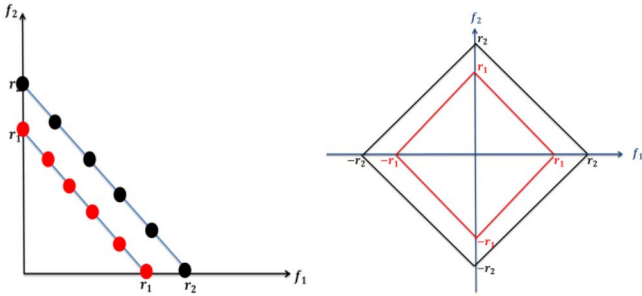


Fig. 10.  $r$  in linear front:  $\sum_{m=1}^M f_m(x) = r$ .

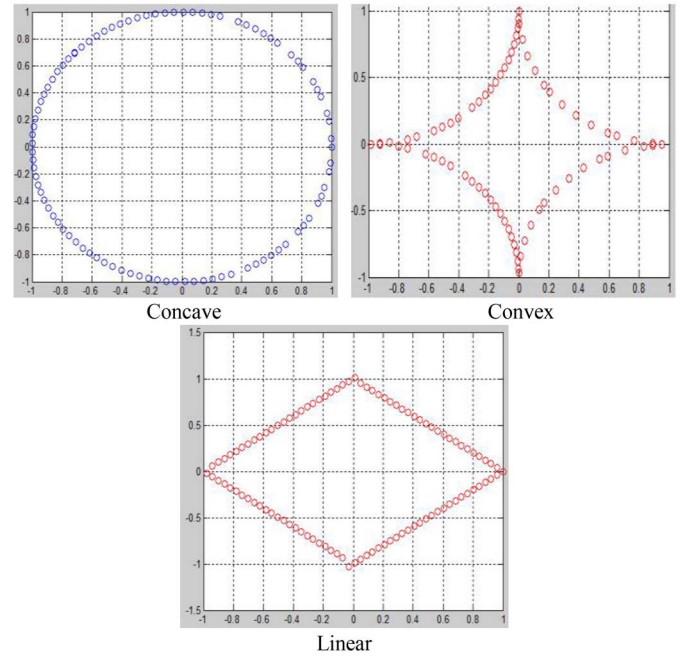


Fig. 11. Three basic fronts in the polar coordinate system.

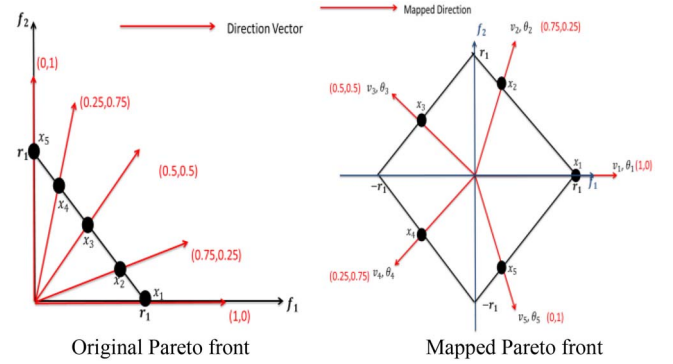


Fig. 12. Mapping linear Pareto front.

space from a 2-D polar coordinate system. For example, a linear approximate front in a high-dimensional space still consists of a few number of linear subfronts in a two-objective space after mapping. Fig. 11 shows three different types of fronts in a two-objective polar coordinate system. The concave front in a high-dimensional space is mapped as four subconcave fronts in the mapped 2-D space for an easy understanding. Similarly, convex front in a high-dimensional space is also mapped as four subconvex fronts in the mapped 2-D space, while the linear front in a high-dimensional space is mapped as four sublinear fronts in the mapped 2-D space.

In order to better explain the whole mapping process, Fig. 12 shows how a linear Pareto front in the original 2-D space is mapped to a 2-D polar coordinate plot.

4) *Visualization of Benchmark Pareto Fronts:* In this section, we will demonstrate the proposed visualization approach through visualizing some well-known benchmark functions. First, in Fig. 13, five widely used bi-objective ZDT test instances are visualized, each of which contains different problem characteristics: convex front in ZDT1, concave front in ZDT2, discrete front in ZDT3, local fronts in ZDT4, and

nonuniform distributed front in ZDT6. Fig. 13 shows both original plots (left) in 2-D objective spaces and mapped plots (right) in the polar coordinate system for ZDT test instances. In each test instance, solutions in the original plot are mapped to positions of solutions with the same color in the mapped plot.

Finally, we look at walking fish group (WFG) problems. One important characteristic of WFG problems is that each objective has different range. Fig. 14 shows both the original plot (left) in a 2-D space and the mapped plot (right) using WFG4 as an example. In the original plot, the Pareto front comes with dissimilar tradeoff, which is reflected by different radial values of solutions in the mapped plot.

5) *Visualization When True Pareto Front is Unknown:* For each individual in a high-dimensional space, the calculation of radial value  $r$  in 2-D coordinate system depends on the approximate Pareto front it locates on. If the front is concave, the corresponding calculation way is  $\sum_{m=1}^M (f_m(x))^2 = r^2$ . If it is convex, the corresponding calculation way is  $\sum_{m=1}^M (r - f_m(x))^2 = r^2$ . If it is linear,  $\sum_{m=1}^M f_m(x) = r$  is applied.

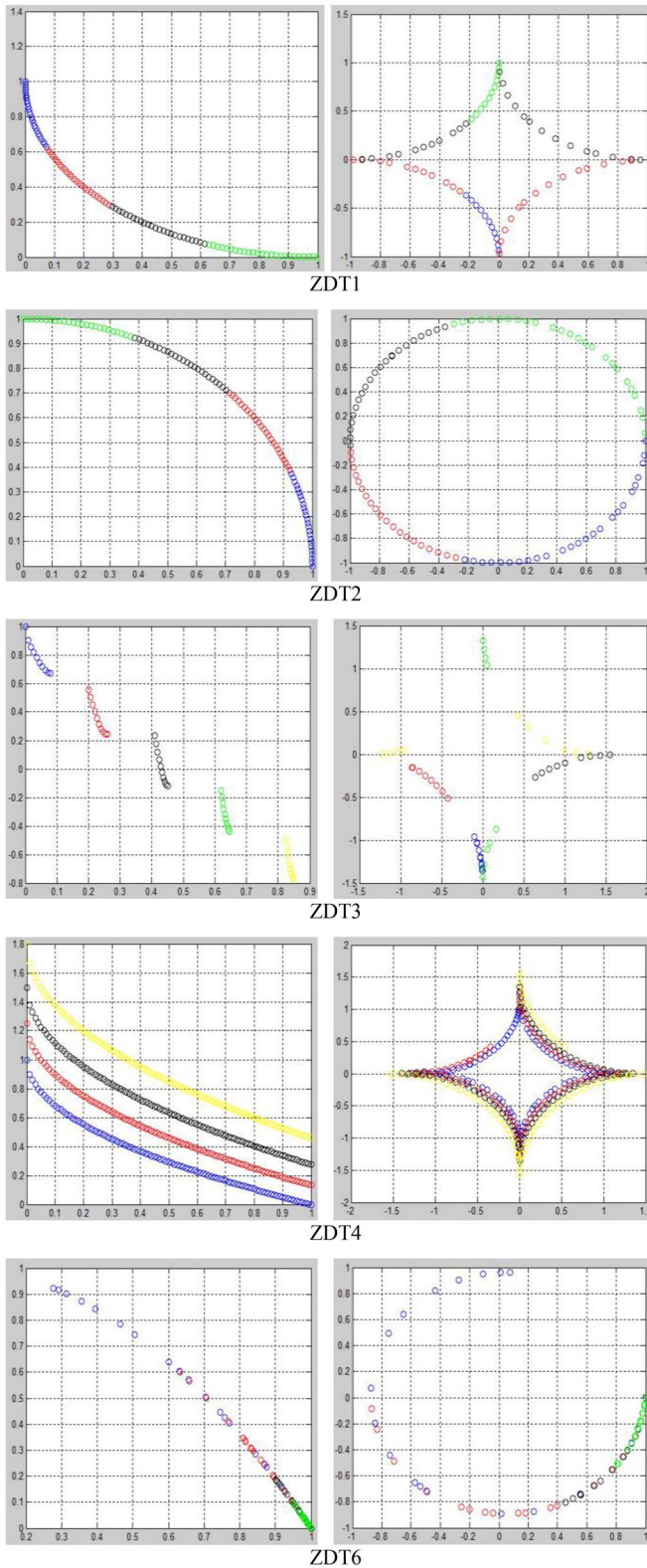


Fig. 13. Visualization of ZDT test instances.

If the true Pareto front is known beforehand, the shape of the approximate Pareto front can be directly determined and its corresponding calculation way is applied to determine  $r$ . If the true Pareto front is unknown, we first determine the shape of the approximate front based on the objective values

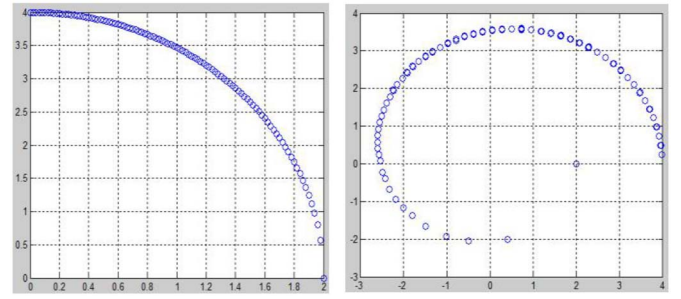


Fig. 14. Visualization of WFG4 test instance.

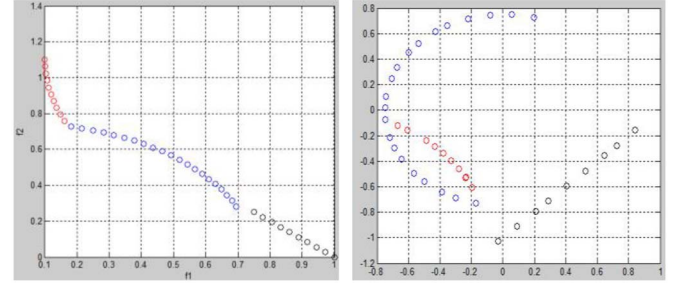


Fig. 15. Visualizing mixed Pareto front.

of individuals on the front. Here, we assume this approximate front is well converged and diversified. It is obvious that an approximate front with poor convergence and diversity cannot provide any useful information for the shape of the true Pareto front and the characteristics of the optimization problem. Then, each calculation way is applied to each individual. Under the same calculation way, if most individuals achieve nearly equal value of  $r$ , the corresponding shape of this way of calculation is considered as the shape of the approximate front.

For the mixed front, although no equal  $r$  exists for most individuals under the same way, nearby individuals will share the similar value of  $r$ 's and the total number of different  $r$ 's is very small, where each  $r$  represents one different shape. Fig. 15 shows one example of calculating  $r$  of each individual on the mixed front, an artificially crafted MOP. On the left side, the original Pareto front contains three different parts: 1) concave (blue); 2) linear (black); and 3) convex (red). This mixed Pareto front is mapped to the front on the right polar plot, where the blue still represents concave part, the black is for linear part, and the red shows convex part. From Fig. 15, nearby individuals in a high-dimensional space contain the similar values of  $r$ 's and they are still located at nearby positions in the mapped plot (in a 2-D polar coordinate system). Meanwhile, each part of Pareto front is continuous in both high-dimensional space and the mapped 2-D Polar coordinate system while it preserves the same shape. Therefore, from the mapped 2-D polar plot, it is easy to visualize how many subparts of this mixed front contains, what the shape of each part is, and how the convergence and diversity performances of each subpart achieves.

In order to make the proposed calculation method more general, for the approximate front with both poor convergence and diversity, where no common  $r$  exists for most individuals



under the same calculation way and all individuals maintain distinct values of  $r$ 's, we choose the calculation way as  $\sum_{m=1}^M (f_m(x))^2 = r^2$  for this front. This way is chosen in that it contains the same form as Euclidean distance which is the most widely used approach to calculate distance between individuals in a high-dimensional objective space.

In summary, it remains a challenging problem to accurately determine the shape of the underlying approximate front. In our experiment, if more than ten individuals on the front achieve a similar  $r$  under one shape, we identify these individuals and construct a subfront with that shape which is a part of the whole approximate front.

As a matter of fact, the way to calculate  $r$  can be considered as a scalarization function, where the input is the original objective values of individuals in a high-dimensional space and the output is radial values in a 2-D polar coordinate system.

6) *Summary of Proposed Visualization Method:* In summary, this visualization method maps individuals from a high-dimensional objective space into a 2-D polar coordinate system with pole (0, 0), where each individual is assigned a radial coordinate value and an angular coordinate value. Radial coordinate reflects convergence performance of each individual and it is determined by the original objective value of each individual and shape of the approximate front in a high-dimensional space. The smaller the radial coordinate value, the closer it is to the true Pareto front. On the other hand, angular coordinate reflects distribution of individuals on the approximate front. It also shows crowdedness in each subregion of a high-dimensional space. The more number of different angular coordinate values among all individuals, the better distribution and spread of the approximate front is. Fig. 16 outlines the whole process of visualization.

This visualization method mainly contributes in four aspects. First, the mapping between a high-dimensional space and a 2-D coordinate system is consistent. It preserves Pareto dominance relationship, retains shape and location of Pareto front, and maintains distribution of solutions. Second, visualization makes it possible to observe the evolution process so as to estimate location, range, and distribution of approximate Pareto front. Third, decision-making is easy and effective. Decision-maker can assess quality of the approximate front and tradeoff between objectives, and easily select preferred solutions. Finally, the application can be scalable to any dimensions, handle a large number of individuals on the front, and simultaneously visualize multiple fronts for visual comparison.

In our method, Euclidean distance is used for calculating distances instead of other  $p$ -norm. Among various choices of  $p$ -norm, Tessema and Yen [40] pointed out that lower value of  $p$  produces better contrast between the maximum and minimum distance in the objective space than larger values of  $p$ . Therefore, the Euclidean distance with the norm two is more effective than the other  $p$ -norm.

### B. Performance Metric Based on Visualization Method

Based on this visualization approach, a new performance metric called  $p$ -metric, is proposed specifically for evaluating

Input: an  $M$ -dimensional approximated front ( $M > 2$ )

Step1: Calculation of Radial Coordinate Value

1) Determine the shape of the approximate front

Concave:  $\sum_{m=1}^M (f_m(x))^2 = r^2$

Convex:  $\sum_{m=1}^M (r - f_m(x))^2 = r^2$

Linear:  $\sum_{m=1}^M f_m(x) = r$

2) If most individuals achieve the same value of  $r$  under one shape, this shape is considered as the shape of the approximate front

3) If most nearby individuals achieve the same value of  $r$  and the total number of different  $r$  is small, this front is considered as the mixed front. Each sub part is calculated independently

4) If most individuals get distinct individuals from others and the total number of different  $r$  is large, treat this front as a concave front

Step2: Calculation of Angular Coordinate Value

1) A group of equally distributed direction vectors are predefined in high-dimensional space. Each vector specifies one sub region

2) Each vector is assigned a fixed angular coordinate value. The angular coordinate difference in degree between two vectors is similar to the distance between both of them in high-dimensional space.

3) For each individual on the approximate front, find the sub region it locates on

for  $j = 1:N$  %N: NO. direction vectors

%w<sub>j</sub>: the jth direction vector

$C_j = \frac{w_j^T f_i}{\|w_j\| \|f_i\|}$  %f<sub>i</sub>: objective value of individual  $i$

end

Find  $j_1 = \arg \max_{j=1:N} C_j$ .

Then  $i$ th individual belongs to  $j_1$ th sub region and its angular coordinate value is equal to that of  $j_1$ th direction vector

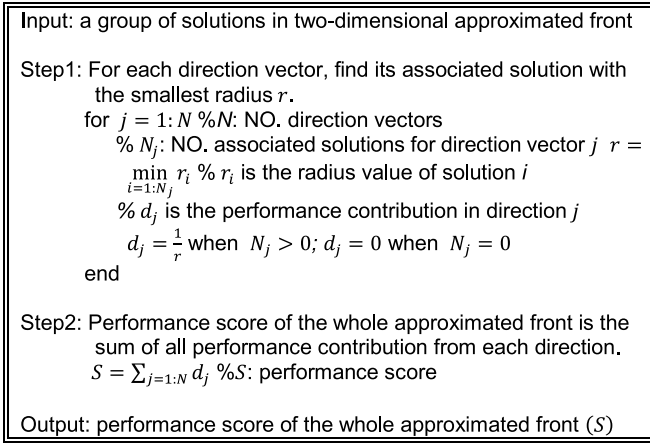
Output: a two-dimensional approximated front with the same shape as the high-dimensional one

Fig. 16. Proposed visualization process.

MaOEAs in both convergence and diversity performances in a high-dimensional objective space. For each direction vector, find its associated approximate solution with the smallest radial value  $r$ . Then, the performance contribution in this direction  $d$  is  $1/r$ . If it does not have an associated solution, performance contribution  $d$  is 0. Finally, performance score of the whole approximate front is the sum of all performance contribution from each direction. The larger the value of metric score, the better the performance of the approximate front is. Fig. 17 shows the detailed steps of implementing the proposed performance metric,  $p$ -metric.

1) *Comparison of  $p$ -Metric With IGD and Hypervolume:* In this paper, IGD and hypervolume indicator (also called  $S$ -metric) are widely applied to compare the performance of MaOEAs. However, both of them are originally designed for comparison in low-dimensional objective spaces and they have distinct disadvantages when applied to high-dimensional objective spaces. On the other hand, these disadvantages are overcome by the proposed  $p$ -metric, which is designed specifically for high-dimensional objective spaces.

First, in a high-dimensional objective space, it is possible that one approximate solution is much better than others

Fig. 17. Details of performance metric:  $p$ -metric.

on the same approximate front. Then the front's IGD and  $S$ -metric scores are only determined by this extreme good solution, which violates the strong outperformance relation defined in [27]. Figs. 18 and 19 show these special instances under both metrics, respectively, that violate strong outperformance relation. On the other hand,  $p$ -metric preserves Pareto dominance optimality in both figures.

In Fig. 18, on the left subfigure, all solutions except  $x_1$  on the approximate front 1 are dominated by at least one solution on the approximate front 2. Only  $x_1$  is nondominated with all solutions on the approximate front 2. However, when IGD metric is applied to measure performance of both approximate fronts, front 1 will obtain a better score (i.e., 0.9) than that of front 2 (i.e., 1.05). This is determined by the way how IGD is calculated. In IGD, each solution in the true Pareto front finds its closest solution on the approximate front, and calculates the distance between them. When it comes to front 1, all solutions in the true Pareto front will choose  $x_1$  as their closest solution on the approximate front. From the left subfigure, the distance between  $x_1$  and each solution on the true front is small. When it comes to front 2, although each solution in the true front can find different approximate solutions, the distance between each pair of them is larger than that between  $x_1$  and each solution on the true front. Therefore, front 1 receives a better score than front 2 under IGD metric. However, front 2 has a better diversity performance and its solutions dominate most of the solutions on front 1. The result of IGD metric clearly violates strong outperformance relation.

In Fig. 19, on the left subfigure, two approximate fronts are compared by using  $S$ -metric. Area enclosed by the approximate front 1 is larger than that of front 2. Therefore, front 1 obtains a better  $S$ -metric score (i.e., 6.625) than that of front 2 (i.e., 4.265). However, all solutions except  $x_1$  on the approximate front 1 are dominated by at least one solution on the approximate front 2. Furthermore, front 2 has a better diversity measure than that of front 1. Therefore, the result of  $S$ -metric also violates strong outperformance relation.

When  $p$ -metric is applied in this condition, approximate front 2 will obtain a better score than that of front 1 based on two points. First, the convergence performance of each solution is determined by its radial coordinate value. Dominated

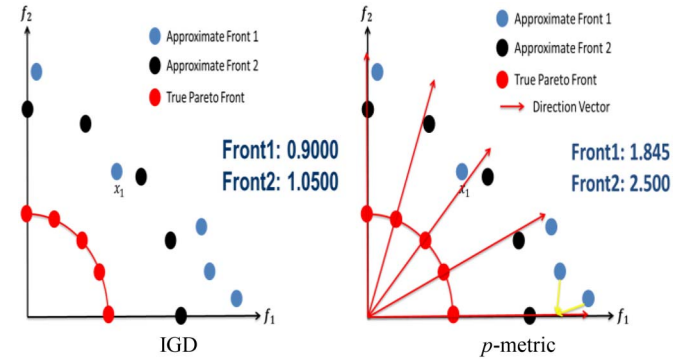
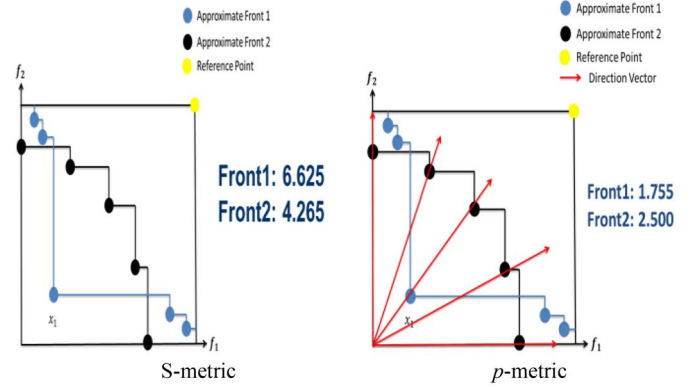


Fig. 18. Instance that IGD score violates strong outperformance relation.

Fig. 19. Instance that  $S$ -metric score violates strong outperformance relation.

solution must contain worse radial coordinate values than those of nondominated ones, which penalizes the dominated solutions. Second, the diversity performance of the whole approximate front is based on angular values of all solutions on that front. If more solutions share the same angular coordinate, then they are crowded in one subregion. Thus, solutions in the crowded area are penalized.

On the right subfigures of both Figs. 18 and 19,  $p$ -metric prefers the approximate front 2 over the approximate front 1. Here, each solution on the approximate front 2 belongs to different direction vector. Therefore, all solutions' radial coordinate values can be counted toward the final performance measure in  $p$ -metric. On the other hand, there are two solutions on the approximate front 1 that belong to the same direction vector. Therefore, only one solution's radial coordinate value can be counted. Furthermore, from the figure, the average radial coordinate value of solutions on the approximate front 1 is larger than that of solutions on front 2. Based on the above discussion,  $p$ -metric prefers front 2 over front 1.

Second, in a high-dimensional space, all solutions on the same front may focus on only one local optimal solution. Therefore, there is no diversity among them. However, this poor performance is not faithfully reflected by the score of IGD and  $S$ -metric. Fig. 20 illustrates this condition in IGD and  $S$ -metrics, respectively.

In Fig. 20, all solutions on the approximate front 1 are located at the same neighborhood. There is nearly no difference among these solutions. However, both metrics (IGD and Hypervolume) still prefer front 1 based on the ways

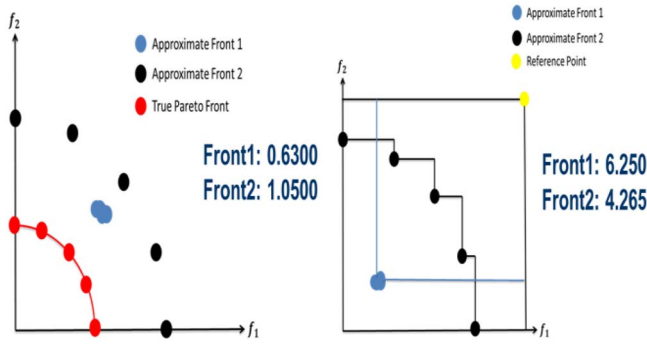


Fig. 20. IGD and  $S$ -metric prefers approximate front 1 over front 2.

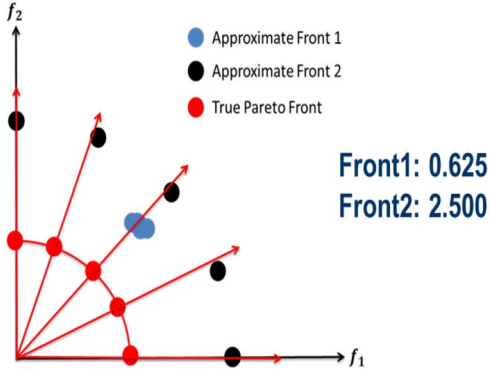


Fig. 21.  $p$ -metric prefers approximate front 2 over front 1.

they are calculated. The extremely poor diversity of front 1 cannot be revealed by scores of both metrics.

In Fig. 21, when  $p$ -metric is applied, all solutions on front 1 belong to the same direction vector while each solution on front 2 belongs to different vector. Although solutions on front 1 contain a little bit smaller average radial coordinate value than that of front 2, front 2 will receive a better performance score using  $p$ -metric due to its better distribution.

The problems highlighted above appear more frequently in MaOPs. Based on the above discussion, both IGD and  $S$ -metric cannot provide accurate comparison results for MaOEAs. The proposed  $p$ -metric, on the other hand, can be applied to make a comprehensive and accurate comparison among MaOEAs.

#### IV. EXPERIMENTAL RESULTS

In this section, five state-of-the-art MaOEAs are chosen to solve 5-D and 10-D benchmark functions DTLZ1–DTLZ7 and generate the approximate fronts for each problem. For each scalable test instance, the proposed visualization approach is then used to map the resulted approximation fronts (produced by all five MaOEAs) from 5-D and 10-D objective spaces into 2-D polar plots for comparison. Afterward, all these fronts are evaluated by  $p$ -metric and two existing metrics, including IGD and  $S$ -metric. Finally, evaluation results from different metrics are ranked to reveal the insights pertaining to the performance of each metric.

##### A. Selected MaOEAs for Comparison

In the experiment, five state-of-the-art MaOEAs are chosen for visual comparison. They are reference-point based many-objective nondominated sorting genetic algorithm (NSGA)-II (NSGA-III) [28],  $\epsilon$ -domination-based MOEA ( $\epsilon$ -MOEA) [29], MOEA based on decomposition (MOEA/D) [30], grid-based evolutionary algorithm (GrEA) [31], and hypervolume estimation algorithm for multiobjective optimization (HypE) [32].

Each algorithm represents one different class of designs in this paper. NSGA-III emphasizes diversity performance and a new diversity-preservation operator is designed to guide the population spread during the evolution process and well-distributed with respect to each other.  $\epsilon$ -MOEA modifies the Pareto-dominance and incorporates grid to preserve diversity. MOEA/D decomposes a MOP into a number of scalar optimization subproblems and optimizes them simultaneously. GrEA exploits the potential of the grid-based approach to strengthen the selection pressure toward the optimal direction, while maintaining an extensive and uniform distribution among solutions. HypE uses the hypervolume indicator to directly assign each individual a fitness value revealing both strengths and weaknesses of it.

##### B. Selected Benchmark Test Problems

Seven widely used scalable many-objective benchmark problems are chosen to evaluate the performance of the MaOEAs considered, DTLZ1–DTLZ7 [33]. In this experiment, chosen MaOEAs are tested in 5-D and 10-D objective spaces of these benchmark problems.

##### C. Parameter Setting in Experiment

The population size in all chosen MaOEAs is set to be 100 for all test instances. The stopping criterion is set at 10 000 generations. Initial populations are generated by uniform random sampling from the search space.

The simulated binary crossover (SBX) and polynomial mutation are used. The crossover operator generates one offspring, which is then modified by the mutation operator. Following the practice in [34], the distribution indexes in SBX and the polynomial mutation are set to be 20. The crossover rate is 1.00, while the mutation rate is  $1/m$  and  $m$  is the number of decision variables. As suggested in [34], for DTLZ1,  $m$  is chosen to be 9 and 14 for 5-D and 10-D problems, respectively, while for DTLZ2–DTLZ7,  $m$  is chosen to be 14 and 19 for 5-D and 10-D problems, respectively. For  $\epsilon$ -MOEA, the parameter setting follows [31]. In MOEA/D [30], the number of the weight vectors in the neighborhood of each weight vector  $T$  is set to be 10. For HypE, according to [32], 10 000 sampling points are used.

##### D. Experimental Results

Detailed comparison results are presented in Tables II and III, where  $p$ -metric, IGD, and  $S$ -metric are applied to compare the performance of five MaOEAs on 5-D and 10-D DTLZ1–DTLZ7, respectively. For the best visualization, it is more effective to choose the number of



TABLE II  
PERFORMANCE OF MaOEAs ON 5-D PROBLEMS

MaOP	Rank	$p$ -metric	IGD	S-metric
DTLZ1	1	GrEA	GrEA	GrEA
	2	NSGA-III	MOEA/D	MOEA/D
	3	HypE	HypE	HypE
	4	MOEA/D	NSGA-III	NSGA-III
	5	$\epsilon$ -MOEA	$\epsilon$ -MOEA	$\epsilon$ -MOEA
DTLZ2	1	GrEA	GrEA	MOEA/D
	2	NSGA-III	$\epsilon$ -MOEA	HypE
	3	$\epsilon$ -MOEA	NSGA-III	NSGA-III
	4	HypE	MOEA/D	GrEA
	5	MOEA/D	HypE	$\epsilon$ -MOEA
DTLZ3	1	GrEA	GrEA	GrEA
	2	HypE	HypE	HypE
	3	NSGA-III	MOEA/D	MOEA/D
	4	MOEA/D	NSGA-III	NSGA-III
	5	$\epsilon$ -MOEA	$\epsilon$ -MOEA	$\epsilon$ -MOEA
DTLZ4	1	GrEA	NSGA-III	MOEA/D
	2	NSGA-III	$\epsilon$ -MOEA	HypE
	3	$\epsilon$ -MOEA	GrEA	NSGA-III
	4	HypE	HypE	GrEA
	5	MOEA/D	MOEA/D	$\epsilon$ -MOEA
DTLZ5	1	MOEA/D	HypE	MOEA/D
	2	NSGA-III	MOEA/D	HypE
	3	HypE	NSGA-III	NSGA-III
	4	$\epsilon$ -MOEA	$\epsilon$ -MOEA	$\epsilon$ -MOEA
	5	GrEA	GrEA	GrEA
DTLZ6	1	MOEA/D	GrEA	MOEA/D
	2	GrEA	MOEA/D	GrEA
	3	NSGA-III	HypE	HypE
	4	HypE	$\epsilon$ -MOEA	NSGA-III
	5	$\epsilon$ -MOEA	NSGA-III	$\epsilon$ -MOEA
DTLZ7	1	GrEA	GrEA	HypE
	2	HypE	HypE	GrEA
	3	NSGA-III	NSGA-III	MOEA/D
	4	MOEA/D	MOEA/D	$\epsilon$ -MOEA
	5	$\epsilon$ -MOEA	$\epsilon$ -MOEA	NSGA-III

TABLE III  
PERFORMANCE OF MaOEAs ON 10-D PROBLEMS

MaOP	Rank	$p$ -metric	IGD	S-metric
DTLZ1	1	GrEA	GrEA	GrEA
	2	MOEA/D	HypE	HypE
	3	HypE	NSGA-III	MOEA/D
	4	NSGA-III	MOEA/D	NSGA-III
	5	$\epsilon$ -MOEA	$\epsilon$ -MOEA	$\epsilon$ -MOEA
DTLZ2	1	GrEA	GrEA	MOEA/D
	2	$\epsilon$ -MOEA	NSGA-III	HypE
	3	HypE	$\epsilon$ -MOEA	NSGA-III
	4	NSGA-III	MOEA/D	GrEA
	5	MOEA/D	HypE	$\epsilon$ -MOEA
DTLZ3	1	GrEA	GrEA	GrEA
	2	MOEA/D	HypE	HypE
	3	HypE	MOEA/D	MOEA/D
	4	$\epsilon$ -MOEA	$\epsilon$ -MOEA	$\epsilon$ -MOEA
	5	NSGA-III	NSGA-III	NSGA-III
DTLZ4	1	GrEA	$\epsilon$ -MOEA	MOEA/D
	2	$\epsilon$ -MOEA	GrEA	HypE
	3	NSGA-III	NSGA-III	NSGA-III
	4	HypE	HypE	GrEA
	5	MOEA/D	MOEA/D	$\epsilon$ -MOEA
DTLZ5	1	HypE	HypE	NSGA-III
	2	NSGA-III	$\epsilon$ -MOEA	HypE
	3	GrEA	NSGA-III	$\epsilon$ -MOEA
	4	$\epsilon$ -MOEA	GrEA	MOEA/D
	5	MOEA/D	MOEA/D	GrEA
DTLZ6	1	NSGA-III	NSGA-III	HypE
	2	HypE	MOEA/D	MOEA/D
	3	MOEA/D	HypE	NSGA-III
	4	$\epsilon$ -MOEA	GrEA	GrEA
	5	GrEA	$\epsilon$ -MOEA	$\epsilon$ -MOEA
DTLZ7	1	HypE	GrEA	HypE
	2	GrEA	HypE	GrEA
	3	$\epsilon$ -MOEA	$\epsilon$ -MOEA	$\epsilon$ -MOEA
	4	MOEA/D	MOEA/D	MOEA/D
	5	NSGA-III	NSGA-III	NSGA-III

direction vectors to be closest to the number of individuals in the approximate fronts. As a result, the number of direction vectors is chosen to be 126 in 5-D problems and 55 in 10-D problems. On each benchmark problem, each algorithm runs 30 times independently to examine the robustness of the three performance metrics. Note that IGD and hypervolume are commonly chosen in this paper to compare the MaOEAs at hand.

Meanwhile, each of Figs. 22–35 shows visualization of the approximate fronts generated by all five MaOEAs on the same mapped 2-D polar plot for visual comparison. In each figure (for the 5-D or 10-D DTLZ1–DTLZ7), “red line” represents the true Pareto front, “blue circle” is the approximate front by GrEA, “black star” represents  $\epsilon$ -MOEA, “yellow square” refers to NSGA-III, “purple diamond” is MOEA/D, while “cyan hexagram” corresponds to HypE. In each figure, under the same DTLZ problem, the mapped 5-D true Pareto front is the same as the mapped 10-D true Pareto front. For example, the true Parent front of 5-D DTLZ1 in Fig. 22 is the same as that of 10-D DTLZ1 in Fig. 23. They appear differently because the scales are different to allow the best visualization of the approximate fronts generated by all five competing MaOEAs.

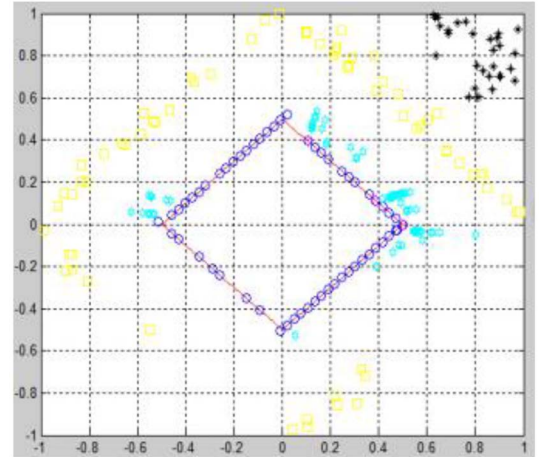


Fig. 22. 5-D DTLZ1.

#### E. Observation and Insight

In 5-D DTLZ1, MOEA/D contains the second best performance among all algorithms under both IGD and S-metric. However, Fig. 22 shows that MOEA/D generates an approximate front (labeled in purple diamond) with all solutions locating at only one portion of the objective space covered by

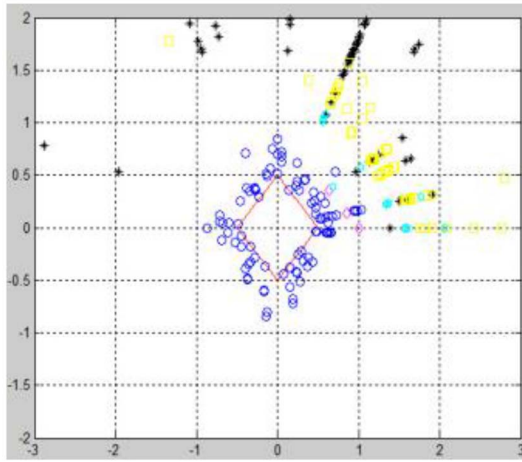


Fig. 23. 10-D DTLZ1.

approximate front of GrEA (blue circle). As validated in [35], MOEA/D is not penalized by its poor diversity under IGD and  $S$ -metric. On the other hand,  $p$ -metric assigns MOEA/D a second worst rank, which properly reflects its poor diversity performance.

In 10-D DTLZ1, from Fig. 23, the approximate fronts obtained by HypE (cyan) and NSGA-III (yellow) are much further away from the true Pareto front. Meanwhile, both of them have poor diversity and they are only located at very few numbers of directions. However, the score of both IGD and  $S$ -metric cannot faithfully reflect these poor convergence and diversity.

In both 5-D and 10-D DTLZ1 which present a linear Pareto front and contain a large number of local fronts [36], GrEA provides the best performance while  $\varepsilon$ -MOEA performs the worst. As we know, both convergence and diversity power of GrEA come from its grid-based design. On the other hand, the convergence power of  $\varepsilon$ -MOEA is based on Pareto-dominance modification (i.e.,  $\varepsilon$ -dominance) while its diversity power comes by restricting each hyperbox with at most a single solution, which is similar to diversity preserving mechanism in a grid-based design. Therefore, it appears that grid-based method for diversity performance better matches with grid-based method for convergence performance than with Pareto-dominance modification method for convergence performance.

In 5-D DTLZ2, IGD metric shows that  $\varepsilon$ -MOEA and MOEA/D perform better than NSGA-III and HypE, respectively. However, in Fig. 24,  $\varepsilon$ -MOEA (black) has similar diversity performance but slightly worse convergence performance than NSGA-III (yellow), while MOEA/D (purple) shows similar convergence performance but worse diversity performance than HypE (cyan). Meanwhile, GrEA contains worse  $S$ -metric score than those of NSGA-III, MOEA/D, and HypE. However, Fig. 24 shows that GrEA (blue) indeed performs better in both convergence and diversity than those three.

In 10-D DTLZ2, IGD metric assigns very different rank values for NSGA-III and HypE. However, the approximate fronts generated by both are very close in Fig. 25. On  $S$ -metric, NSGA-III receives a better rank than GrEA which is in conflict with the visualization result shown in Fig. 25.

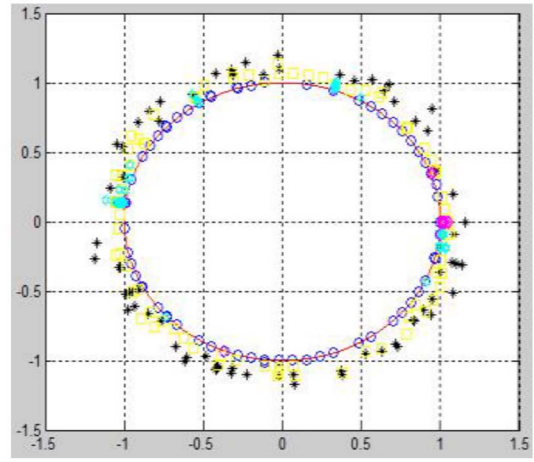


Fig. 24. 5-D DTLZ2.

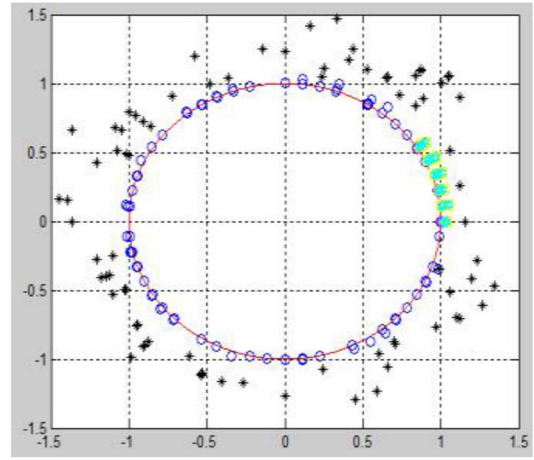


Fig. 25. 10-D DTLZ2.

DTLZ3 also introduces a large number of local Pareto fronts [36]. Again, GrEA shows its best performance in both 5-D and 10-D problems, while  $\varepsilon$ -MOEA has an inferior performance. Therefore, it supports our observation from DTLZ1 that grid-based design for diversity performance better matches with grid-based design for convergence performance than Pareto-dominance modification method for convergence performance. Furthermore, in Figs. 26 and 27, it is easy to observe that HypE (cyan),  $\varepsilon$ -MOEA (black), and NSGA-III (yellow) can only converge to several different local Pareto fronts.

In 5-D DTLZ4, MOEA/D and HypE have better performance under  $S$ -metric. However, Fig. 28 shows that both algorithms generate the approximate fronts with very poor diversity. Furthermore, their convergence performance is also worse than that of GrEA.

In 10-D DTLZ4,  $\varepsilon$ -MOEA (black) obtains a better rank under IGD than GrEA. However, from Fig. 29, both algorithms generate the approximate fronts with similar diversity performance, while GrEA (blue) achieves a better convergence performance than  $\varepsilon$ -MOEA. Under  $S$ -metric, NSGA-III (yellow), MOEA/D (purple), and HypE (cyan) receive better scores than that of GrEA. However, Fig. 29 shows that

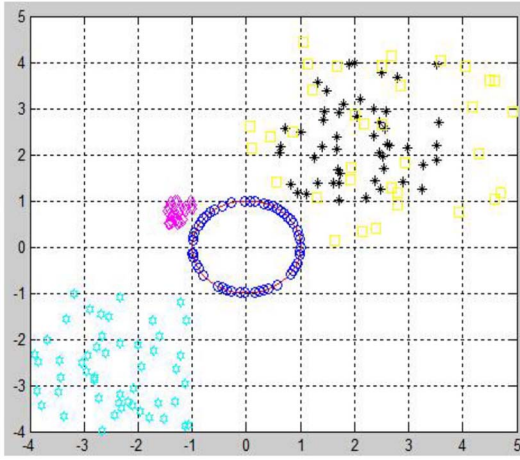


Fig. 26. 5-D DTLZ3.

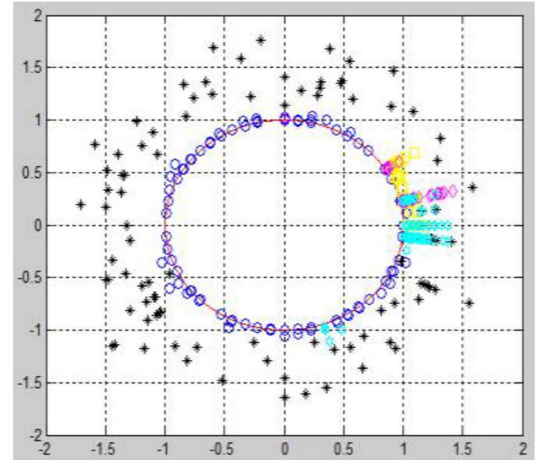


Fig. 29. 10-D DTLZ4.

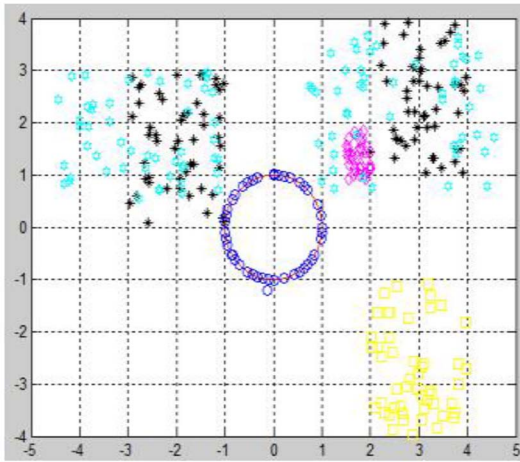


Fig. 27. 10-D DTLZ3.

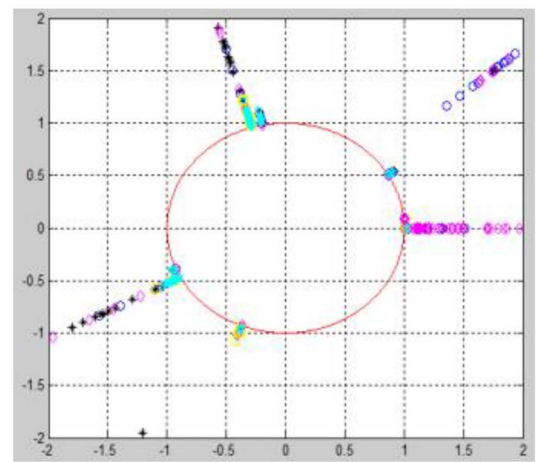


Fig. 30. 5-D DTLZ5.

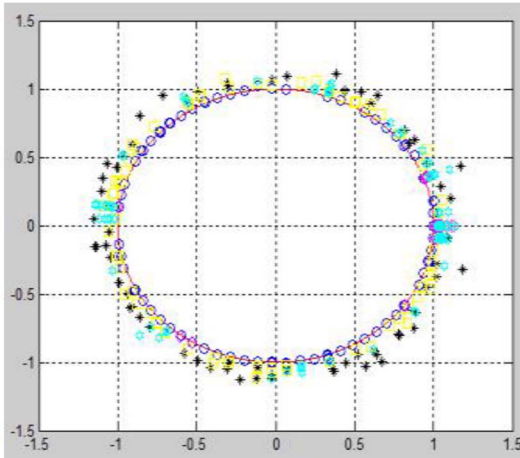


Fig. 28. 5-D DTLZ4.

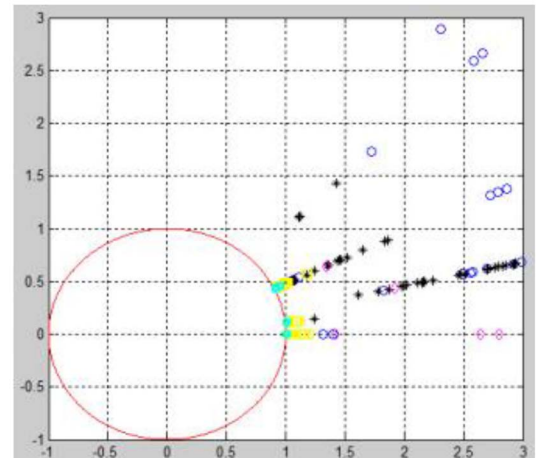


Fig. 31. 10-D DTLZ5.

GrEA performs indeed better than them in both convergence and diversity.

From [28], DTLZ4 generates a nonuniform distribution of solutions along the Pareto front. GrEA with its best rank result shows that the grid-based design with the same grid length in each dimension is still effective in solving problems

with nonuniform distribution of the Pareto front, which is also implied by experiment results in [31].

In 10-D DTLZ5, IGD metric shows that  $\varepsilon$ -MOEA is better than NSGA-III. However, we can draw an opposite conclusion from Fig. 31. In DTLZ5, the Pareto front is a degenerated hypersurface [36]. The diversity-emphasis method,



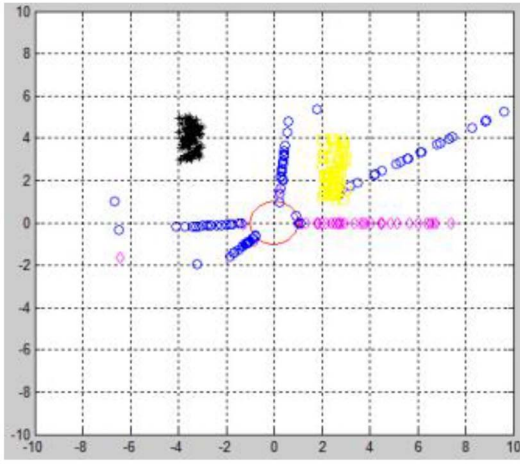


Fig. 32. 5-D DTLZ6.

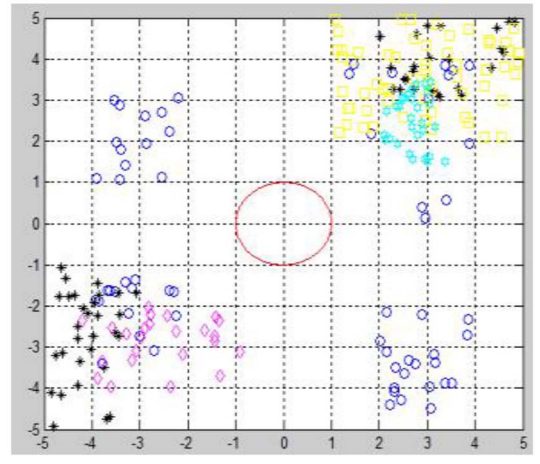


Fig. 34. 5-D DTLZ7.

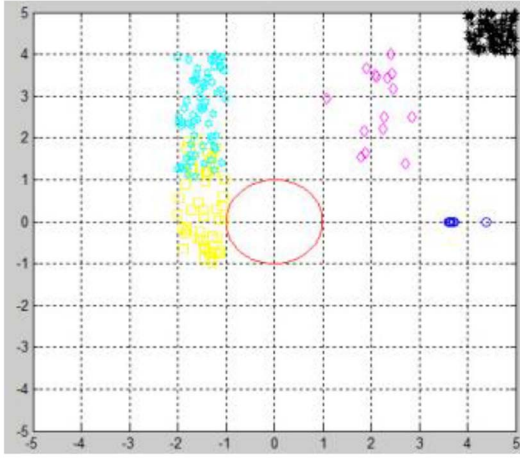


Fig. 33. 10-D DTLZ6.

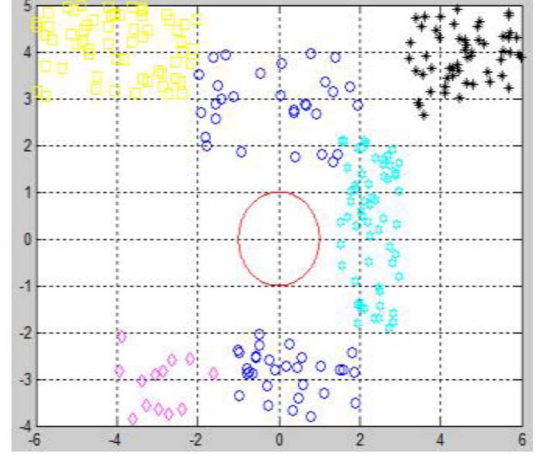


Fig. 35. 10-D DTLZ7.

NSGA-III (yellow), and indicator-based method, HypE (cyan), show better performance than others. Here, GrEA (blue) performs much worse than itself in other problems. It seems that grid-based design has difficulties handling problems with degenerated hypersurface. Meanwhile, Figs. 30 and 31 imply that all MaOEAs chosen cannot attain both well convergence and diversity performance in DTLZ5.

From [31], DTLZ6 has a large number of local Pareto fronts and disconnected Pareto-optimal regions. Again, the difficulty of  $\epsilon$ -MOEA in handling lots of local Pareto fronts results into a poor performance in DTLZ6. Although GrEA has shown its ability in dealing with lots of local fronts in DTLZ1, it displays a poor performance in 10-D problem. Therefore, the disconnected Pareto-optimal regions plus high-dimensional space make it difficult for grid-based method to achieve a well converged and diversified approximate front. Meanwhile, in Fig. 32, it is easy to observe that a lot of approximate solutions generated by GrEA (blue), MOEA/D (purple), and NSGA-III (yellow) converge to several local Pareto fronts.

DTLZ7 is constructed with the constrained surface approach [36]. The Pareto front of DTLZ7 is the intersection of a straight line and a hyperplane. Results in Figs. 34 and 35 support the observation from [36]: the tested

MaOEAs may find it difficult to converge to the Pareto front and to maintain a good distribution of solutions along it. However, performance metric alone cannot reflect this observation results and validate this detection. Visualization method allows us to observe both convergence and diversity performances.

In addition to discussions in Section III-B, these observations confirm that both IGD and  $S$ -metric cannot provide a comprehensive and accurate comparison among MaOEAs in a MaOP. The newly proposed metric,  $p$ -metric on the other hand, can be an effective alternative to draw a fair assessment.

## V. CONCLUSION

In a high-dimensional objective space, visualization presents an essential tool in developing MaOEAs and in solving MaOPs. A new visualization approach is proposed herein. It maps individuals from a high-dimensional objective space into a 2-D polar coordinate system while preserving Pareto dominance relationship, retaining shape and location of Pareto front, and maintaining distribution of them.

From the resulted polar plot, a decision-maker can observe the evolution process, estimate location, range, and distribution of Pareto front, assess quality of the approximate front and tradeoff between objectives, and easily select preferred solutions. Furthermore, its applications can be scalable to any dimensions, handle a large number of individuals on front, and simultaneously visualize multiple fronts for comparison. Based on this visualization method, a performance metric, named  $p$ -metric, is proposed. The convergence of the approximate front is measured by radial values of all population members on that front. Meanwhile, the diversity performance of the approximate front is mainly determined by niche count of each subregion in a high-dimensional space. Experimental results show that it can provide a comprehensive and consistent comparison among MaOEAs.

In future work, we would like to extend the idea of visualization and performance metric to constrained MaOPs because most real-world problems involve constraints and dynamic character. For the obtained approximate front to be usable, all constraints must be satisfied. In this paper, many efforts have been devoted to constrained [33]–[35] and dynamic [36]–[38] problems. However, there is little publications that refer to the high-dimensional constrained and dynamic problems. Therefore, the idea of constraint satisfaction should be incorporated in MaOP. First, the mapping process in visualization method preserves not only Pareto dominance relationship and local distances among solutions in high-dimensional spaces, but also the degree of how each solution satisfies the constraints [39]–[44]. Then, the performance metric score of each solution should be based on the fusion of its convergence and diversity measures, and also constraint satisfying degree.

## REFERENCES

- [1] T. Tutar and B. Filipic, "Visualization of Pareto front approximations in evolutionary multiobjective optimization: A critical review and the projection method," *IEEE Trans. Evol. Comput.*, vol. 19, no. 2, pp. 225–245, Apr. 2015.
- [2] D. Brockhoff and E. Zitzler, "Objective reduction in evolutionary multi-objective optimization: Theory and applications," *Evol. Comput.*, vol. 17, no. 2, pp. 135–166, Jun. 2009.
- [3] D. K. Saxena, J. A. Duro, A. Tiwari, K. Deb, and Q. Zhang, "Objective reduction in many-objective optimization: Linear and nonlinear algorithms," *IEEE Trans. Evol. Comput.*, vol. 17, no. 1, pp. 77–99, Feb. 2013.
- [4] R. J. Lygoe, M. Cary, and P. J. Fleming, "A many-objective optimization decision-making process applied to automotive diesel engine calibration," in *Simulated Evolution and Learning (LNCS 6457)*. Berlin, Germany: Springer, 2010, pp. 638–646.
- [5] A. Inselberg, *Parallel Coordinates: Visual Multidimensional Geometry and its Applications*. New York, NY, USA: Springer, 2009.
- [6] A. Pryke, S. Mostaghim, and A. Nazemi, "Heatmap visualisation of population based multi objective algorithms," in *Proc. Int. Conf. Evol. Multi-Criterion Optim.*, Matsushima, Japan, 2007, pp. 361–375.
- [7] M. F. Ashby, "Multi-objective optimization in material design and selection," *Acta Mater.*, vol. 48, no. 1, pp. 359–369, Jan. 2000.
- [8] P. E. Hoffman, G. G. Grinstein, K. Marx, I. Grosse, and E. Stanley, "DNA visual and analytic data mining," in *Proc. IEEE Vis. Conf.*, Phoenix, AZ, USA, 1997, pp. 437–441.
- [9] T. Kohonen, *Self-Organizing Maps*. Berlin, Germany: Springer, 2001.
- [10] J. J. Valdes and A. J. Barton, "Visualizing high dimensional objective spaces for multi-objective optimization: A virtual reality approach," in *Proc. IEEE Congr. Evol. Comput.*, Singapore, 2007, pp. 4199–4206.
- [11] D. Lowe and M. E. Tipping, "Feed-forward neural networks and topographic mappings for exploratory data analysis," *Neural Comput. Appl.*, vol. 4, no. 2, pp. 83–95, Jun. 1996.
- [12] T. Okabe, Y. Jin, and B. Sendhoff, "A critical survey of performance indices for multi-objective optimisation," in *Proc. IEEE Congr. Evol. Comput.*, Canberra, ACT, Australia, 2003, pp. 878–885.
- [13] G. G. Yen and Z. He, "Performance metrics ensemble for multiobjective evolutionary algorithms," *IEEE Trans. Evol. Comput.*, vol. 18, no. 1, pp. 131–144, Feb. 2014.
- [14] D. J. Walker, R. M. Everson, and J. E. Fieldsend, "Visualizing mutually nondominating solution sets in many-objective optimization," *IEEE Trans. Evol. Comput.*, vol. 17, no. 2, pp. 165–184, Apr. 2013.
- [15] S. Obayashi and D. Sasaki, "Visualization and data mining of Pareto solutions using self-organizing map," in *Proc. IEEE Congr. Evol. Multi-Criterion Optim.*, Faro, Portugal, 2003, pp. 796–809.
- [16] J. B. Tenenbaum, V. Silva, and J. C. Langford, "A global geometric framework for nonlinear dimensionality reduction," *Science*, vol. 290, no. 5500, pp. 2319–2323, Dec. 2000.
- [17] I. Borg and P. J. F. Groenen, *Modern Multidimensional Scaling: Theory and Applications*. New York, NY, USA: Springer, 2005.
- [18] K. C. Tan, T. H. Lee, and E. F. Khor, "Evolutionary algorithms for multi-objective optimization: Performance assessments and comparisons," *Artif. Intell. Rev.*, vol. 17, no. 4, pp. 251–290, Jun. 2002.
- [19] D. A. Van Veldhuizen, "Multiobjective evolutionary algorithms: Classifications, analyses, and new innovations," Ph.D. dissertation, Air Force Inst. Technol., Wright-Patterson AFB, Dayton, OH, USA, 1999.
- [20] C.-K. Goh and K. C. Tan, "A competitive-cooperative coevolutionary paradigm for dynamic multiobjective optimization," *IEEE Trans. Evol. Comput.*, vol. 13, no. 1, pp. 103–127, Feb. 2009.
- [21] P. Czyzszak and A. Jaszkiewicz, "Pareto simulated annealing—A meta-heuristic technique for multiple-objective combinatorial optimization," *J. Multi-Criteria Decis. Anal.*, vol. 7, no. 1, pp. 34–47, Jan. 1998.
- [22] J. R. Schott, "Fault tolerant design using single and multicriteria genetic algorithm optimization," M.S. thesis, Dept. Aeronaut. Astron., Massachusetts Inst. Technol., Cambridge, MA, USA, 1995.
- [23] J. Wu and S. Azarm, "Metrics for quality assessment of a multiobjective design optimization solution set," *J. Mech. Design*, vol. 123, no. 1, pp. 18–25, Mar. 2001.
- [24] E. Zitzler, L. Thiele, and K. Deb, "Comparison of multiobjective evolutionary algorithms: Empirical results," *IEEE Trans. Evol. Comput.*, vol. 8, no. 2, pp. 173–195, Jun. 2000.
- [25] E. Zitzler and L. Thiele, "Multiobjective optimization using evolutionary algorithms—A comparative case study," in *Proc. Int. Conf. Parallel Probl. Solving Nature*, Amsterdam, The Netherlands, 1998, pp. 292–301.
- [26] Z. He, G. G. Yen, and J. Zhang, "Fuzzy-based Pareto optimality for many-objective evolutionary algorithms," *IEEE Trans. Evol. Comput.*, vol. 18, no. 2, pp. 269–285, Apr. 2014.
- [27] M. P. Hansen and A. Jaszkiewicz, "Evaluating the quality of approximations to the non-dominated set," Institute of Mathematical Modelling, Tech. Univ. Denmark, Lyngby, Denmark, Tech. Rep. IMM-REP-1998-7, 1998.
- [28] K. Deb and H. Jain, "An evolutionary many-objective optimization algorithm using reference-point based non-dominated sorting approach, part I: Solving problems with box constraints," *IEEE Trans. Evol. Comput.*, vol. 18, no. 4, pp. 602–622, Aug. 2014.
- [29] K. Deb, M. Mohan, and S. Mishra, "Evaluating the  $\epsilon$ -domination based multi-objective evolutionary algorithm for a quick computation of Pareto-optimal solutions," *Evol. Comput.*, vol. 13, no. 4, pp. 501–525, Feb. 2005.
- [30] Q. Zhang and H. Li, "MOEA/D: A multiobjective evolutionary algorithm based on decomposition," *IEEE Trans. Evol. Comput.*, vol. 11, no. 6, pp. 712–731, Dec. 2007.
- [31] S. Yang, M. Li, X. Liu, and J. Zheng, "A grid-based evolutionary algorithm for many-objective optimization," *IEEE Trans. Evol. Comput.*, vol. 17, no. 5, pp. 721–736, Oct. 2013.
- [32] J. Bader and E. Zitzler, "HypE: An algorithm for fast hypervolume based many-objective optimization," *Evol. Comput.*, vol. 19, no. 1, pp. 45–76, Mar. 2011.
- [33] K. Deb, L. Thiele, M. Laumanns, and E. Zitzler, "Scalable multi-objective optimization test problems," in *Proc. IEEE Congr. Evol. Comput.*, Honolulu, HI, USA, pp. 825–830, 2002.
- [34] K. Deb, A. Pratab, S. Agrawal, and T. Meyarivan, "A fast and elitist multiobjective genetic algorithm: NSGA-II," *IEEE Trans. Evol. Comput.*, vol. 6, no. 2, pp. 182–197, Apr. 2002.
- [35] Z. He and G. G. Yen, "Performance metrics ensemble for many-objective evolutionary algorithms," *Adv. Eng. Softw.*, vol. 76, pp. 1–8, Oct. 2014.

- [36] S. Huband, P. Hingston, L. Barone, and L. While, "A review of multiobjective test problems and a scalable test problem toolkit," *IEEE Trans. Evol. Comput.*, vol. 10, no. 5, pp. 477–506, Oct. 2006.
- [37] H.-L. Liu, F. Gu, and Q. Zhang, "Decomposition of a multiobjective optimization problem into a number of simple multiobjective subproblems," *IEEE Trans. Evol. Comput.*, vol. 18, no. 3, pp. 450–455, Jun. 2014.
- [38] S. Venkatraman and G. G. Yen, "A generic framework for constrained optimization using genetic algorithms," *IEEE Trans. Evol. Comput.*, vol. 9, no. 4, pp. 424–435, Aug. 2005.
- [39] Y. G. Woldesenbet, G. G. Yen, and B. G. Tessema, "Constraint handling in multi-objective evolutionary optimization," *IEEE Trans. Evol. Comput.*, vol. 13, no. 3, pp. 514–525, Jul. 2009.
- [40] B. Tessema and G. G. Yen, "An adaptive penalty formulation for constrained evolutionary optimization," *IEEE Trans. Syst., Man, Cybern. A, Syst., Humans*, vol. 39, no. 3, pp. 565–578, May 2009.
- [41] Y. G. Woldesenbet and G. G. Yen, "Dynamic evolutionary algorithm with variable relocation," *IEEE Trans. Evol. Comput.*, vol. 13, no. 3, pp. 500–513, Jun. 2009.
- [42] G. G. Yen and W. F. Leong, "Dynamic multiple swarms in multiobjective particle swarm optimization," *IEEE Trans. Syst., Man, Cybern. A, Syst., Humans*, vol. 39, no. 4, pp. 890–911, Jul. 2009.
- [43] G. G. Yen and H. Lu, "Dynamic multiobjective evolutionary algorithm: Adaptive cell-based rank and density estimation," *IEEE Trans. Evol. Comput.*, vol. 7, no. 3, pp. 253–274, Jun. 2003.
- [44] K. M. Woldemariam and G. G. Yen, "Vaccine enhanced artificial immune system for multimodal function optimization," *IEEE Trans. Syst., Man, Cybern. B, Cybern.*, vol. 40, no. 1, pp. 218–228, Feb. 2010.



**Zhenan He** received the B.E. degree in automation from University of Science and Technology Beijing, Beijing, China, in 2008 and the M.S. degree in electrical and computer engineering from Oklahoma State University (OSU), Stillwater, OK, USA, in 2011.

He is with the School of Electrical and Computer Engineering, OSU. His research interests include multiobjective optimization using evolutionary algorithms, neural networks, and machine learning.



**Gary G. Yen** (S'87–M'88–SM'97–F'09) received the Ph.D. degree in electrical and computer engineering from University of Notre Dame, Notre Dame, IN, USA, in 1992.

He joined Oklahoma State University, Stillwater, OK, USA, in 1997, where he is currently a Professor with the School of Electrical and Computer Engineering. He was with the U.S. Air Force Research Laboratory, Albuquerque, NM, USA. His research is supported by the Department of Defense, Department of Energy, Environmental Protection

Agency, the National Aeronautics and Space Administration, the National Science Foundation, and Process Industry. His research interests include intelligent control, computational intelligence, conditional health monitoring, signal processing, and their industrial/defense applications.

Dr. Yen was a recipient the Andrew P. Sage Best Transactions Paper Award from the IEEE Systems, Man and Cybernetics Society in 2011 and the Meritorious Service Award from the IEEE Computational Intelligence Society in 2013. He was an Associate Editor of *IEEE Control Systems Magazine*, *IEEE TRANSACTIONS ON CONTROL SYSTEMS TECHNOLOGY*, *Automatica*, *Mechantronics*, *IEEE TRANSACTIONS ON SYSTEMS, MAN, AND CYBERNETICS—PART A: SYSTEMS AND HUMANS*, *IEEE TRANSACTIONS ON SYSTEMS, MAN, AND CYBERNETICS—PART B: CYBERNETICS*, and *IEEE TRANSACTIONS ON NEURAL NETWORKS*. He is currently an Associate Editor of the *IEEE TRANSACTIONS ON EVOLUTIONARY COMPUTATION* and *International Journal of Swarm Intelligence Research*. He served as the General Chair for the 2003 IEEE International Symposium on Intelligent Control held in Houston, TX, USA, and the 2006 IEEE World Congress on Computational Intelligence held in Vancouver, BC, Canada, the Vice President for the Technical Activities from 2005 to 2006, the President of the IEEE Computational Intelligence Society from 2010 to 2011, and the Founding Editor-in-Chief of *IEEE Computational Intelligence Magazine* from 2006 to 2009.